

Article

Enhancing the Electrochemical Performance of ZnO-Co₃O₄ and Zn-Co-O Supercapacitor Electrodes Due to the In Situ Electrochemical Etching Process and the Formation of Co₃O₄ Nanoparticles

Khabibulla Abdullin ^{1,2}, Maratbek Gabdullin ³, Zhanar Kalkozova ^{1,*}, Vladislav Kudryashov ⁴,
Mojtaba Mirzaeian ^{5,*}, Kassym Yelemessov ⁶, Dinara Baskanbayeva ⁶ and Abay Serikkanov ^{2,7}

- ¹ National Nanotechnology Laboratory of Open Type (NNLOT), Al-Farabi Kazakh National University, Al-Farabi Avenue 71, Almaty 050040, Kazakhstan; kh.abdullin@physics.kz
- ² Satbayev University, Institute of Physics and Technology, Almaty 050013, Kazakhstan; a.serikkanov@sci.kz
- ³ Kazakh-British Technical University, Tole bi Street, 59, Almaty 050000, Kazakhstan; gabdullin@physics.kz
- ⁴ Lab of Renewable Energy, National Laboratory Astana, Nazarbayev University, Astana 010000, Kazakhstan; kudryashov.post@gmail.com
- ⁵ School of Computing, Engineering and Physical Sciences, University of the West of Scotland, Paisley PA1 2BE, UK
- ⁶ Institute of Energy and Mechanical Engineering named after A. Burkitbayev, Satbayev University, 22 Satbaev Str., Almaty 050013, Kazakhstan; k.yelemessov@satbayev.university (K.Y.); d.baskanbayeva@satbayev.university (D.B.)
- ⁷ National Academy of Sciences of the Republic of Kazakhstan under the President of the Republic of Kazakhstan, Shevchenko Str. 28, Almaty 050010, Kazakhstan
- * Correspondence: zhanar.kalkozova@kaznu.edu.kz (Z.K.); mojtaba.mirzaeian@uws.ac.uk (M.M.)



Citation: Abdullin, K.; Gabdullin, M.; Kalkozova, Z.; Kudryashov, V.; Mirzaeian, M.; Yelemessov, K.; Baskanbayeva, D.; Serikkanov, A. Enhancing the Electrochemical Performance of ZnO-Co₃O₄ and Zn-Co-O Supercapacitor Electrodes Due to the In Situ Electrochemical Etching Process and the Formation of Co₃O₄ Nanoparticles. *Energies* **2024**, *17*, 1888. <https://doi.org/10.3390/en17081888>

Academic Editor: Huang Zhang

Received: 19 March 2024

Revised: 8 April 2024

Accepted: 10 April 2024

Published: 16 April 2024



Copyright: © 2024 by the authors. Licensee MDPI, Basel, Switzerland. This article is an open access article distributed under the terms and conditions of the Creative Commons Attribution (CC BY) license (<https://creativecommons.org/licenses/by/4.0/>).

Abstract: Zinc oxide (ZnO) and materials based on it are often used to create battery-type supercapacitor electrodes and are considered as promising materials for hybrid asymmetric supercapacitors. However, when creating such electrodes, it is necessary to take into account the instability and degradation of zinc oxide in aggressive environments with a non-neutral pH. To the best of our knowledge, studies of the changes in the properties of ZnO-containing electrodes in alkaline electrolytes have not been carried out. In this work, changes in the structure and properties of these electrodes under alkaline treatment were investigated using the example of ZnO-containing composites, which are often used for the manufacturing of supercapacitor electrodes. Supercapacitor electrodes made of two materials containing ZnO were studied: (i) a heterogeneous ZnO-Co₃O₄ system, and (ii) a hexagonal h-Zn-Co-O solid solution. A comparison was made between the structure and properties of these materials before and after in situ electrochemical oxidation in the process of measuring cyclic voltammetry and galvanostatic charge/discharge. It has been shown that the structure of both nanoparticles of the heterogeneous ZnO-Co₃O₄ system and the h-Zn-Co-O solid solution changes due to the dissolution of ZnO in the alkaline electrolyte 3.5 M KOH, with the short-term alkaline treatment producing cobalt and zinc hydroxides, and long-term exposure leading to electrochemical cyclic oxidation–reduction, forming cobalt oxide Co₃O₄. Since the resulting cobalt oxide nanoparticles are immobilized in the electrode structure, a considerable specific capacity of 446 F g^{−1} or 74.4 mA h g^{−1} is achieved at a mass loading of 0.0105 g. The fabricated hybrid capacitor showed a good electrochemical performance, with a series resistance of 0.2 Ohm and a capacitance retention of 87% after 10,000 cycles.

Keywords: supercapacitor electrode; ZnO-based composite; cobalt oxide nanoparticles

1. Introduction

After iron oxide, zinc oxide (ZnO) is the most abundant metal oxide which has unique and tunable properties such as a high level of electrical conductivity, intense photoluminescence, and piezoelectric properties, and strong dependence of its bulk properties on the

surface condition [1–4]. These properties can be further tuned and improved by doping zinc oxide with other transition metals [4–10]. The synthesis of ZnO through various methods makes it possible to control the morphology of its nanoparticles and obtain both nanoparticles of various shapes and arrays of nanorods on various substrates. A number of recent reviews have demonstrated the promise of zinc oxide, as well as compounds and composites based on it, as attractive materials for a variety of practical uses [11–14]. The application of ZnO and its composites in photocatalysis, water splitting, and Oxygen Evolution Reaction is discussed in [15–19]. Many reviews and research studies have discussed the use of ZnO in gas and chemical sensors [20–22], and in bio-sensors [23–31]. Different articles and reviews have also been published on the prospects of its applications in photodetectors [32–37] and solar cells [38–40].

Discussions on the use of ZnO and different compounds based on it, such as ZnO-CoO, as well as ZnO-CoO core-shell nanostructures for energy storage/ conversion, lithium-ion batteries, and supercapacitors, can be found in recent reviews [41–45]. Yan et al., prepared a three-dimensional nanostructure of CoO/ZnO-NrGO using a simple solvothermal method followed by freeze-drying, in which CoO/ZnO nanoclusters were fixed on N-doped 3D reduced graphene oxide as the anode material for a lithium-ion battery [46]. The material demonstrated a gravimetric capacity of 1494 mA h g^{-1} at a current density of 0.1 A g^{-1} and 600 mA h g^{-1} at current density of 2 A g^{-1} after 1000 cycles and showed a decrease in the volumetric expansion of CoO and ZnO, with an increased transport rate for the Li ions.

Undoped ZnO, used as electroactive material in supercapacitor electrodes, exhibits specific capacitances of 200 F g^{-1} [47], 314 F g^{-1} [48], 162 F g^{-1} or 22.5 mA h g^{-1} [49], 55 F g^{-1} [50], and 86.4 F g^{-1} [51] for samples synthesized by various methods. It has been shown that the specific capacity of ZnO depends on the morphology of its nanoparticles and its defect structure, varying within the range of 65 F g^{-1} to $\sim 330 \text{ F g}^{-1}$ [52]. In [53], undoped ZnO synthesized by the non-aqueous sol-gel route showed a specific capacitance of 776 F g^{-1} at a high current density of 4 A g^{-1} .

It can be seen that such a wide spread of specific capacitance values can, in some cases, be explained by the low mass loadings available on a nickel foam substrate. If the mass of the active substance is 1 mg cm^{-2} or less, the contribution of the nickel substrate to the electrode capacitance can significantly overestimate the specific capacitance value.

Different studies have shown that doping ZnO with other compounds can lead to an increase in the specific capacitance. For example, a study by Alver and Tanriverdi showed that the introduction of boron into the ZnO growth solution when a hydrothermal method was used for the synthesis of ZnO increases its specific capacitance to $\sim 230 \text{ F g}^{-1}$, compared to a specific capacitance of 55 F g^{-1} for undoped ZnO [50]. Reddy et al. also studied the effect the concentration of Ni as dopant on the structure, optical properties, photoelectrochemical (PEC) water splitting capabilities, and supercapacitor applications of ZnO and observed that 1.5% Ni-doped ZnO demonstrates a specific capacitance of $\sim 96 \text{ F g}^{-1}$ with a coulombic efficiency of $\sim 99.5\%$ at an applied scan rate of 10 mV s^{-1} [54]. Erdemir et al. utilized a simple solution-combustion method for the synthesis of fluorine-doped ZnO particles using glycine as a fuel. The obtained ZnO-based materials were used as an electroactive material in the fabrication of electrodes and the supercapacitive performance of the electrodes was investigated in an electrochemical cell using a 3 M KOH electrolyte. It was found that the fluorine doping improves the microstructure and supercapacitive performances of the ZnO particles and increases the specific capacitance of ZnO from 3.39 F g^{-1} to 12.2 F g^{-1} with approximately 91.5% of its initial capacitance being retained after 4000 charge/discharge cycles at a scan rate of 10 mV s^{-1} [55]. Ali et al. have shown that doping ZnO with molybdenum in a so-called “single-step hydrothermal process” increases the specific capacitance of ZnO from $\sim 1300 \text{ F g}^{-1}$ to $\sim 2300 \text{ F g}^{-1}$ [56]. Pallavolu et al. also studied the influence of molybdenum and vanadium doping of ZnO, when synthesized in the exchange reaction, on its electrochemical performance. Mo- and V-doped ZnO electrodes exhibited specific capacitances up to $\sim 30\%$ higher than the specific capacitance of undoped ZnO, which amounted to 555 F g^{-1} and 585 F g^{-1} for Mo-ZnO

and V-ZnO, respectively [57]. Investigating the impact of Cd doping on the electrochemical performance of ZnO-based electrodes, Angelin et al. have shown that a 9 wt% Cd-doped ZnO electrode exhibits a specific capacitance of 627 F g^{-1} at a current density of 1 A g^{-1} and significant cycling stability after 5000 GCD cycles as compared to a specific capacitance of 314 F g^{-1} for the bare ZnO electrode [48].

The synthesis of zinc compounds with other transition metals, such as Mn, Mo, Ni, etc., as well as with carbon materials, makes it possible to achieve high specific capacitance values, and several ZnO-based systems have been tested as an electrode material for supercapacitors [14,41,43]. Solid solutions of quaternary transition metal oxides such as NiCoMoZnO_x have also been tested as a material for supercapacitors and have shown promising results with a capacity of $0.41 \text{ mA h cm}^{-2}$, corresponding to the CF value of 2.12 F cm^{-2} obtained for NiCoMoZnO_x electrodes [58]. ZnO@MnO_2 core-shell nanofibers were synthesized by a combination of the electrospinning method followed by hydrothermal treatment [59]. A specific capacitance of 907 F g^{-1} at a current density of 0.6 A g^{-1} was achieved due to the better conductivity of the zinc oxide nanofibers used as the core supporting material and the pseudo-capacitive nature of the MnO_2 nanoflakes. Binder-free ZnO@MnO_2 electrodes on Ni foam have shown a specific capacity of 423.5 F g^{-1} at 0.5 A g^{-1} with an excellent cyclic stability [60].

Composites containing zinc and cobalt oxides in various forms have also shown a good performance when used as electrode materials for supercapacitors [14,41–47]. Using a ZnO/CoO composite as the electroactive material in an electrode exhibits an enhanced super-capacitive performance of 85 mA h g^{-1} ($\sim 681 \text{ F g}^{-1}$), attained at a significantly high current density of 20 A g^{-1} [49]. Such characteristics were attributed to the higher electrical conductivity of ZnO, and its interconnected porous structure, which ensured the fast transportation of ions and electrons. The mass of ZCO composites loaded on the Ni foam is approximately 1 mg cm^{-2} .

Tajik et al. synthesized a ZnCo_2O_4 mixed-transition metal oxide nanostructure through a simple method called a “solid-state reaction”. The supercapacitive performances of the material when used as the working electrode in 6 M KOH in an electrochemical cell consisting of three electrodes showed a specific capacitance of 844 F g^{-1} [61]. Abebe et al. developed binder-free electrodes made of ZnO/ Co_3O_4 nanosheets on a Ni foam used as the current collector through a two-step method using chemical bath deposition (CBD) [47]. The nanosheets showed a specific capacitance of 940 F g^{-1} which was measured using the CV method at a scan rate of 5 mV s^{-1} in a 1 M KOH electrolyte in an electrochemical cell. The capacitance of the nanosheets determined by the galvanostatic charge/discharge measurements was 740 F g^{-1} at a current density of 0.75 A g^{-1} . This was notably higher than the single-component capacities of 785 F g^{-1} and 200 F g^{-1} obtained for Co_3O_4 and ZnO electrodes, respectively, due to the large surface area and high electrical conductivity of the nanocomposite structure. Dutta et al. [62] synthesized $\text{Zn}_{1-x}\text{Co}_x\text{O}$ samples ($x = 0, 0.02, 0.04$) using a wet precipitation method. The $\text{Zn}_{0.6}\text{Co}_{0.4}\text{O}$ electrode demonstrated a high electrochemical performance in a supercapacitor, reported as “a specific capacitance of 697 F g^{-1} , a power density of 1026 W kg^{-1} , and an energy density of 24 W h kg^{-1} , with a good cyclic stability”. In [63], a Zn-Co-O@CoS core-shell material was synthesized by the deposition of CoS nanosheets on the surface of ZnO/ Co_3O_4 nanowires. The core-shell material provided a high specific capacity of $\sim 330 \text{ mA h g}^{-1}$, higher than the specific capacitance of the original ZnO electrode by a factor of seven. ZnO/CoO@NiCoS nano hybrids synthesized through a three-step method provided a specific capacity of 934 C g^{-1} (1868 F g^{-1}), which is 5.5 times greater than the specific capacity of the original ZnO electrode [64]. This nano hybrid also demonstrated an improved power density and a high energy density.

Some recent publications show continued interest in ZnO-based supercapacitors. Kumar et al. [65] have shown that the specific capacitance of ZnO nanostructures doped with 3% iron (Fe) is 286 F g^{-1} at 10 mV s^{-1} , where 85.0% of the capacitance value of the $\text{Zn}_{0.97}\text{Fe}_{0.03}\text{O}$ electrode was retained after 2000 cycles. In a study of the enhanced electro-

chemical behavior of ZnO electrode materials for supercapacitor applications by Zenasni et al., a polypyrrole@ZrO₂-ZnO (PPy@ZrO₂-ZnO) electrode demonstrated a specific capacitance and an energy density of 395.3 F g⁻¹ and 508.5 W h kg⁻¹, respectively, with 90% retention of the capacitance after cycling up to 4000 cycles [66]. The development of hybrid supercapacitor devices with high performances based on Mn-doped and copper-doped zinc oxide is reported in [67]. The hybrid supercapacitor had the highest specific capacity of 151 F g⁻¹ along with an energy density of 84 W h kg⁻¹ and a power density of 75 kW kg⁻¹. Altaf et al. have developed “all-solid-state photo-supercapacitors” based on graphene oxide/zinc oxide (GO/ZnO) composites [68]. The specific capacity of GO/ZnO composites increased after UV irradiation and reached ~6.6 F g⁻¹. A symmetrical metal oxide-based supercapacitor was also developed by Chauhan et al. [69]. The capacitor uses a novel electrode with a vanadium pentoxide/zinc oxide (V₂O₅/ZnO) stacked structure and is optically responsive. Mubeen et al. [70] reported novel ZnO/CuS composite materials with different CuS ratios used as the electrode materials for supercapacitor applications. The capacitive performances of ZnO/CuS electrodes were measured in a three-electrode cell, where a capacitance of 487 F g⁻¹, a high-power density of 13,448 W kg⁻¹, and a maximum energy density of 26 W h kg⁻¹ were achieved. Using a sol-gel synthesis route, Shaheen et al. synthesized ZnO/CuO and ZnO/CuO/rGO heterostructure and electrophoretically deposited it on an indium tin oxide substrate as a thin uniform layer [71]. The heterostructure showed a specific capacitance of 2305 F g⁻¹ at a voltage rate of 2 mV s⁻¹ and 1235 F g⁻¹ at a current density of 5 A g⁻¹. The specific capacitance of asymmetric supercapacitors using ZnO nanosheets on Ni foam (ZnO@NF) as the positive electrode and activated carbon (AC) on Ni foam (AC@NF) as the negative electrode reaches up to 87 F g⁻¹ at 1 A g⁻¹ and the supercapacitors exhibit an energy density of 28 W h kg⁻¹ and a power density of 839 W kg⁻¹ [72]. Considering all these extensive works on the utilization of ZnO as an electrode material for supercapacitor applications shows that using ZnO-based materials as electrode materials for supercapacitors is currently attracting significant and sustained interest.

It should be noted that, for the safe and continual operation of a device, its electrode materials must be stable when operating in electrolytes and demonstrate reversibility of the acquired properties under conditions of electrochemical redox reactions. However, despite a considerable amount of attention being paid to its usage as the electrode material for supercapacitors, the chemical resistance of ZnO and some materials based on it is often overestimated and is far from the chemical resistance of materials that is required when they are used in aggressive environments under electrochemical oxidation conditions. According to Pern et al., ZnO is not a sufficiently resistant material and gradually degrades even when used in humid air as transparent conducting oxides (TCOs); therefore, ZnO layers require protection from atmospheric exposure [73]. ZnO is highly soluble in many acids and alkalis, such as KOH and NaOH. According to Chen et al., at pH = 6–14, ZnO is not fully stable and the reaction of ZnO with NaOH can produce ZnOH⁺, Zn(OH)³⁻ and Zn(OH)₄²⁻ [74]. At high alkali concentrations (i.e., >0.1 M), which are used in supercapacitors, the reaction of ZnO and M (M = Na, K) at pH > 12 will form water-soluble zincates such as MZn(OH)₃ or M₂Zn(OH)₄ [64]. In a supercapacitor with ZnO-based electrodes, ZnO dissolves in reactions with the electrolyte during charging, and the dissolution of ZnO continues until the alkaline electrolyte is saturated with zincates. However, as the surface layer involved in creating the capacitance degrades with discharge, the properties of the supercapacitor electrode undergo significant changes and this process continues with the cycling of the device.

Thus, when preparing supercapacitor electrodes using ZnO and other related materials, it is important to take into account the change in the structure of ZnO-containing electrodes due to their interaction with the electrolyte. However, as far as we are concerned, despite the enormous number of studies on supercapacitors with ZnO electrodes in alkaline electrolytes, no investigations have been conducted on the changes in the structure of the electrodes during the operation of supercapacitors yet.

In order to investigate the effect of changes in the structure of ZnO electrodes in a supercapacitor when exposed to an alkaline electrolyte, as well as due to in situ electrochemical etching, we prepared two ZnO-based materials—a ZnO/Co₃O₄ nanocomposite and a hexagonal Zn-Co-O solid solution. The structure and phase composition of the electrodes fabricated from these materials were then investigated before and after capacitance tests in a 3.5 M KOH electrolyte in an electrochemical cell. It was found that the phase composition of the electrodes changes sharply as a result of both simple exposure to an alkaline electrolyte and after in situ oxidation. The contribution of the ZnO phase and hexagonal Zn-Co-O to the electrode composition decreases, and, with short-term exposure to alkali, the Co(OH)₂ phase appears, while a continuous cycle of 10,000 cycles in the galvanostatic charge/discharge mode leads to the formation of a nanocrystalline phase such as Co₃O₄ or ZnCo₂O₄. The specific capacitance of the electrode material was 446 F g⁻¹ at a mass loading of 0.0105 g. An asymmetric capacitor was also manufactured using such electrodes as a positive electrode and an activated carbon electrode as a negative electrode. The capacitor demonstrated a capacitance of 1.48 F at a mass loading of 0.025 g for the positive electrode and at a voltage of 1.4 V. A high specific capacitance is formed because Co₃O₄ or ZnCo₂O₄ nanoparticles immobilized into the electrode structure are formed during the reaction of the electrode material (ZnO-Co₃O₄ and h-Zn-Co-O) with the electrolyte. The nanoparticles have a high and active specific surface area due to the in situ synthesis.

2. Materials and Methods

2.1. Materials

Reagent-grade Zn(NO₃)₂·6H₂O zinc nitrate (NZn), Co(NO₃)₂·6H₂O cobalt nitrate (NCo), C₄H₆CoO₄·4H₂O cobalt acetate (AcCo), C₆H₁₂N₄ hexamethylenetetramine (HMT), (NH₂)₂CO carbamide, N-methyl-2-pyrrolidone (NMP), PTFE dispersion 60 wt% in H₂O (Sigma Aldrich, Gillingham, Dorset, UK), PVDF Kynar, and activated carbon (Fuzhou Yihuan Carbon Co., Fuzhou, China) were used for the synthesis of electrode materials. MilliQ water (18.2 MΩ·cm) used for synthesis of samples was produced by an AQUA-MAX—Ultra 370 Series ultrapure water purification system (YL Instrument Co., Anyang, Korea).

2.2. Synthesis of the ZnO-Co₃O₄ and h-Zn-Co-O

The main goal of this research was to study the behavior of ZnO-containing materials when exposed to an alkaline electrolyte, as well as to investigate the changes in the structure and properties of electrodes made from the synthesized materials during their operation in the 3.5 M KOH electrolyte in an electrochemical cell, which is often used in supercapacitors. To accomplish this, we synthesized ZnO-Co₃O₄ and h-Zn-Co-O composites, since these ZnO-containing composites are considered as promising electrode materials for supercapacitor applications [35,43–47,49,51–72].

Zinc–cobalt oxide nanoparticles (Zn-Co-O) and h-Zn-Co-O NPs were obtained through chemical deposition at 90 °C followed by annealing at 300 °C. The growth solution had a molar ratio of the cobalt, zinc, HMT, and carbamide used as precursors of 1:1:1:5, respectively. A higher carbamide content was chosen to fully utilize the cobalt precursors, since, at a lower carbamide content, the pinkish growth solution after synthesis indicates the presence of dissolved divalent cobalt.

Precursors of cobalt (NCo or AcCo) and zinc (NZn) were dissolved in an equimolar ratio in 400 mL of water. HMT and carbamide were dissolved separately. The solution containing cobalt and zinc precursors was heated to 90 °C under stirring in a water bath. Then, the solutions of HMT and carbamide were added to this solution. All syntheses were carried out in the growth solution at a fixed concentration of 0.01 M for cobalt, zinc, and HMT. The molar concentration of carbamide in the solution was 0.05 M. The synthesis was carried out within 24 h under gentle stirring at 90 °C. The reaction was stopped by lowering the temperature to room temperature; then, the precipitates in the form of a pink powders were washed with deionized water several times, filtered, and then dried at 80 °C.

The resulting pink powders were calcined in an atmosphere of hydrogen, nitrogen, or air for 1 h. To maintain small particle sizes, annealing temperatures of 275–300 °C were used.

Annealing in the air was carried out in a muffle furnace. For annealing in hydrogen or nitrogen, a quartz tube furnace was used, where annealing was carried out in a gas flowrate of 2 L per hour, at a rate of 5 degrees min^{-1} . After annealing, the furnace was left to cool to room temperature naturally.

The composition of samples synthesized by the chemical bath deposition method depends on the conditions of synthesis and subsequent annealing. At a fixed equimolar ratio of cobalt (NCo or AcCo) and zinc (NZn) precursors, the phase composition depended on two main factors: (i) the type of cobalt precursor (NCo or AcCo) used, where the corresponding syntheses and obtained samples are designated as NCo+NZn or AcCo+NZn, and (ii) the atmosphere (i.e., oxygen or oxygen-free) under which the annealing was carried out. It was found that if cobalt (NCo) and zinc (NZn) nitrates were used as precursors, then samples containing a mixture of ZnO and Co_3O_4 phases were synthesized after annealing at a temperature of 300 °C within an air atmosphere, as shown below. The same samples, after annealing at 300 °C in a nitrogen or H_2 atmosphere, consisted of a hexagonal solid solution of h-Zn-Co-O with an admixture of the Co_3O_4 phase. Synthesis using cobalt acetate (AcCo) and zinc nitrate (NZn) as precursors followed by annealing in air at 300 °C made it possible to obtain samples of a hexagonal solid solution of h-Zn-Co-O with an admixture of the Co_3O_4 phase, and after annealing in nitrogen or H_2 at 300 °C, a pure h-Zn-Co-O phase without traces of Co_3O_4 phase was obtained. The obtained samples were treated in an alkaline electrolyte by mixing 0.5 g of the sample and 5 mL of a 3.5 M KOH solution; the treatment time was varied, and then the powder was washed in water and dried.

2.3. Characterization Techniques

A MiniFlex X-ray diffractometer (Rigaku) operating with $\text{CuK}\alpha$ radiation at a wavelength of 1.5418 Å using an accelerating voltage of 40 kV and a current of 15–40 mA was used to study the phase structure of the samples. The morphology of the samples was examined using a Quanta 200i 3D scanning electron microscope (SEM) (FEI) and JEM-2100 transmission electron microscopy (TEM) (JEOL). An NEXSA X-ray photoelectron spectrometer (Thermo Scientific, Waltham, MA, USA) was used to investigate the chemical composition of the materials. Raman spectra were studied on an NTEGRA Spectrometer (NT-MDT, Zelenograd, Russia) with solid-state laser excitation at a wavelength of 473 nm.

2.4. Electrode Preparation

To manufacture electrodes from $\text{ZnO}/\text{Co}_3\text{O}_4$ and h-Zn-Co-O on nickel foam, a preliminarily annealed powder or as-synthesized sample was used. The required volume of NMP solvent was added to an agate mortar, followed by the addition of PVDF and acetylene black (CB), and the mixture was stirred, and then the powdered sample was added. The mass ratio of the sample, carbon black, and PVDF was 8:1:1. Nickel foam (NF) substrates with a thickness of 2 mm were cut into pieces with an area of 1 cm^2 , boiled in acetone, and immersed in 10% nitric acid for a few seconds, followed by rinsing in water and drying for complete cleaning of their surface. $\text{ZnO}-\text{Co}_3\text{O}_4$ /NF or h-Zn-Co-O/NF pseudocapacitor electrodes were prepared by pre-weighting the NF substrate first, followed by applying the required amount of dispersion or paste containing the sample to the substrate, and drying the electrode in a vacuum oven at 60 °C for at least 3 h. The operation was repeated several times to obtain samples with the required mass loading. Then, the resulting electrode was pressed at ~10 MPa and the mass of the electroactive material was worked out from the difference in mass between the manufactured electrode after electrochemical studies and the initial substrate. For the preparation of an activated carbon (AC) electrode, the required amount of AC powder was mixed with acetylene black (CB), used as the conductivity enhancer, and PVDF, used as the binder, in a weight ratio of 8:1:1. The mixture was ground in an agate mortar, then mixed with the NMP solution and the resulting paste was applied

on the surface of a piece of clean nickel foam as the substrate, and dried in a vacuum oven; then, the AC/NF electrode was pressed.

2.5. Electrochemical Analysis of Electrode and Hybrid Supercapacitor

The electrochemical properties of the prepared electrodes were studied with a P-40X-FRA-24M potentiostat (Elins) in a three-electrode system consisting of a working electrode (prepared electrodes), a reference electrode (Ag/AgCl), and a counter electrode (platinum), using a 3.5 M KOH solution as the electrolyte. To study the electrochemical characteristics of the asymmetric hybrid supercapacitor, which had a negative capacitor-type electrode and a positive battery-type oxide electrode, a two-electrode cell of the Swagelok type was used; the contact area of the electrode was 1 cm², and a filter paper or a hydrophilic PTFE filter was used as the separator. The positive electrode consisted of NF with a deposited sample, where an AC/NF electrode was used as the negative electrode. The electrochemical characteristics of the materials and the performance of the asymmetric hybrid supercapacitor were studied through different measurements using cyclic voltammetry (CV), galvanostatic charge/discharge (GCD), and electrochemical impedance spectroscopy (EIS) methods in the frequency range of 0.1 Hz–500 kHz at a sinusoidal potential amplitude of 20 mV.

3. Results and Discussion

3.1. Morphology and Structure

Curve 1 in Figure 1a shows the XRD pattern of the sample obtained from the synthesis of NCo+NZn. As a result of annealing the as-obtained sample at 300 °C within an air atmosphere, a ZnO-Co₃O₄ system was formed. Narrow XRD patterns of the ZnO phase and broad reflections of Co₃O₄ characterize the particle sizes, indicating that the ZnO-Co₃O₄ powder sample consists of Co₃O₄ nanocrystals and larger ZnO crystals. SEM images of this sample (Figure 2a) confirm the XRD data. The well-faceted particles can be attributed to ZnO, while the Co₃O₄ phase is represented by thin lamellar particles.

The XRD curve of the sample obtained after the synthesis of AcCo+NZn followed by annealing in air is shown in Figure 1b, curve 1. This sample contains the h-Zn-Co-O and ZnO phases with a small admixture of Co₃O₄. The h-Zn-Co-O phase is characterized by fairly broad reflections, coinciding in position with the reflections of ZnO, while narrow lines correspond to ZnO particles. Note that the pure h-Zn-Co-O phase without impurities of ZnO and Co₃O₄ particles can be obtained using AcCo and NZn precursors after annealing the as-obtained sample in hydrogen or nitrogen, as will be shown below.

A mixture of h-Zn-Co-O and ZnO nanoparticles is formed when using NCo and NZn precursors and after annealing the as-obtained sample in hydrogen, as can be seen in Figure 1c, curve 1. In this case, the Co₃O₄ phase is not observed.

The phase composition of samples containing h-Zn-Co-O and ZnO changed significantly even after short-term alkaline treatment, as can be seen in Figure 1a–c, curves 2. As seen in Figure 1 and Figure S1 (Supplementary Material), after treating a sample containing ZnO and Co₃O₄ with an alkali, the intensity of the ZnO reflections decreased, while the intensity of the Co₃O₄ reflections remained unchanged for this sample (Figure 1a, curve 2). The intensities of the h-Zn-Co-O phase's XRD reflections decrease (Figure 1b,c) after treatment in alkali for 10 min, and the hydroxides Co(OH)₂ (PDF card No. 01-089-8616) and Zn₂Co₃(OH)₁₀·2H₂O (PDF card No. 00-021-1477) appear as a result of the alkaline treatment.

Figure 3 shows TEM images of samples obtained from AcCo+NZn precursors after annealing in air, before (Figure 3a) and after 30 min of treatment in a KOH solution (Figure 3b). A comparison between Figure 3a,b, shown on the same scale, clearly show that the average particle sizes in Figure 3b are much smaller than those in Figure 3a due to the disappearance of the large faceted ZnO crystals after KOH treatment. This signifies that alkaline etching leads to the fact that the contribution of the ZnO and h-Zn-Co-O phases decreases, and nanocrystals of cobalt hydroxides and oxides are formed. Thus, even

short-term etching of ZnO-Co₃O₄ and h-Zn-Co-O powder samples results in a significant alteration to the phase composition of the samples.

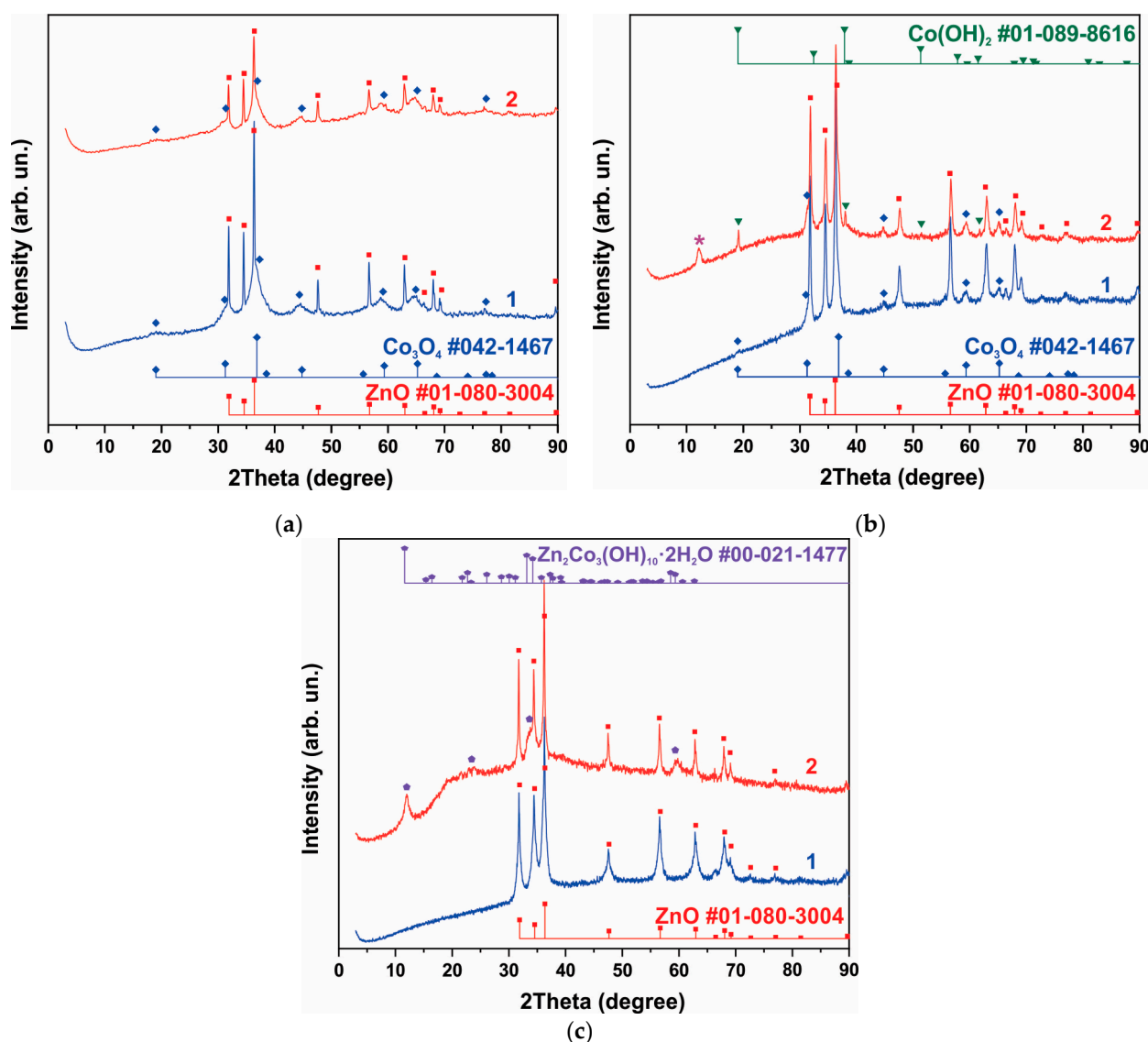


Figure 1. XRD patterns of samples containing phases of ZnO and Co₃O₄ (a), h-Zn-Co-O, ZnO and Co₃O₄. The reflection corresponding to the Zn₂Co₃(OH)₁₀·2H₂O phase (PDF Card No.: 00-021-1477) is marked with an asterisk in figure (b), and h-Zn-Co-O and ZnO (c). Curve 1 corresponds to the XRD pattern of the samples before treatment, and curve 2 is the XRD pattern after alkaline treatment in 3.5 M KOH for 10 min.

The effect of in situ electrochemical action can differ significantly from simple etching in an electrolyte. This effect of in situ electrochemical action on ZnO-Co₃O₄/NF and h-Zn-Co-O/NF electrodes was investigated using the CV and GCD methods. Figure 4a shows the XRD patterns of the electrodes that were annealed at 300 °C within air (curves 1 and 2), or in hydrogen at 300 °C (3 and 4). Curves 1 and 3 correspond to the as-prepared electrodes, where all of their XRD reflections correspond to a h-Zn-Co-O solid solution. The half-width of reflections for samples annealed in hydrogen is noticeably higher than the half-width of the reflections of the samples after annealing in air. Using the Scherrer formula, the average crystallite sizes in the samples were estimated as 19.2 nm and 10.9 nm for the samples after annealing in air and hydrogen, respectively. Curves 2 and 4 in Figure 4a show XRD patterns of the electrodes after CV measurements for 10 min in the

3.5 M KOH electrolyte. Figure 4a shows that, within 10 min, the in situ electrochemical action has already led to a noticeable change in the phase composition of the h-Zn-Co-O samples. This occurs as, firstly, the intensity of reflections from the hexagonal structure of the ZnO type has decreased noticeably, especially in the sample annealed in hydrogen, and secondly, new XRD reflections corresponding to the $\text{Co}(\text{OH})_2$ lattice (PDF Card No.: 01-089-8616) have appeared. The presence of another additional peak at 11.5° for these samples can be attributed to the hydroxide phase of $\text{Zn}_2\text{Co}_3(\text{OH})_{10} \cdot 2\text{H}_2\text{O}$ (PDF Card No.: 00-021-1477). The average crystallite sizes, estimated using the Scherrer formula, also changed to the values of 16.1 nm and 13.8 nm for the samples after annealing in air and hydrogen, respectively. Thus, the effect of short-term electrochemical exposure in situ is similar to the effect of treatment in an alkaline solution.

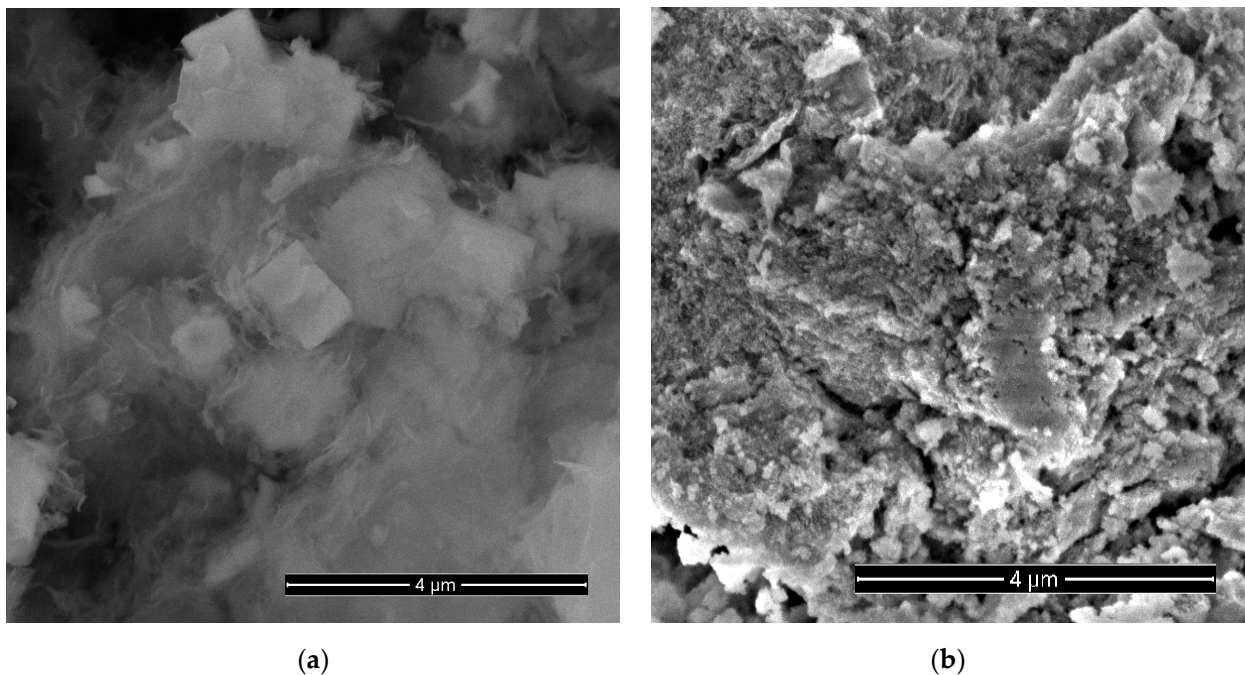


Figure 2. SEM images of a sample obtained using cobalt and zinc nitrates (NCo and NZn) as precursors, followed by annealing at 300 °C in air (a) and after etching in 3.5 M KOH for 10 min (b).

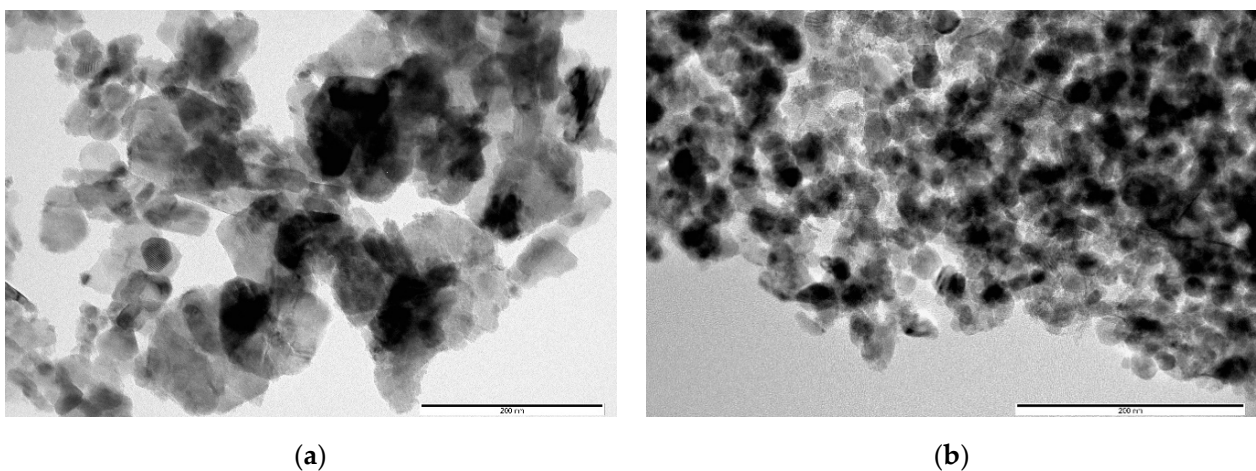


Figure 3. TEM images of AcCo+NZn samples before (a) and after treatment in KOH (b). The scale bar corresponds to 200 nm.

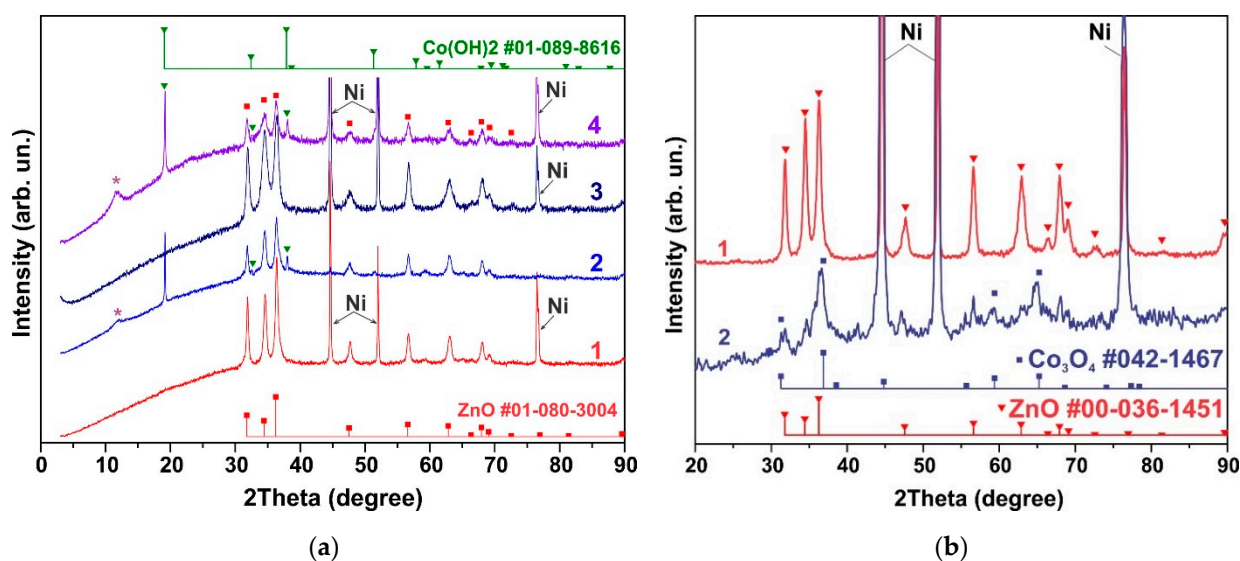


Figure 4. h-Zn-Co-O/NF electrodes annealed in air at 300 °C (curves 1 and 2) and in hydrogen at 300 °C (3 and 4) before CV measurements (1, 3) and after CV measurements in 3.5 M KOH for ~10 min. The reflection corresponding to the $\text{Zn}_2\text{Co}_3(\text{OH})_{10} \cdot 2\text{H}_2\text{O}$ phase (PDF Card No.: 00-021-1477) is marked with an asterisk in figure (a). XRD pattern of h-Zn-Co-O electrode before and after GCD measurements for 300 cycles (b).

Figure 4b shows the change in structure after long-term (24 h) GCD measurements. As can be seen in Figure 4b, the XRD patterns of the h-Zn-Co-O disappear and only the Co_3O_4 nanoparticles' XRD pattern is present. The average size of Co_3O_4 crystallites, estimated using the Scherrer formula, turned out to be 5.5 ± 0.7 nm. Thus, the intensity of h-Zn-Co-O reflections decreases, and cobalt hydroxides appear in the initial stage of in situ oxidation; subsequently, only reflections of the Co_3O_4 fine nanocrystals remain.

3.2. Raman Spectra

As mentioned above, the samples, which were obtained from the synthesis using cobalt acetate (AcCo) and zinc nitrate (NZn) as precursors followed by annealing in nitrogen or hydrogen atmosphere at 300 °C, showed only XRD reflections of the h-Zn-Co-O phase. The Co_3O_4 and ZnO phases, as well as other phases, were not observed. Since a growth solution with an equimolar composition of zinc and cobalt was used in the synthesis, the composition of the obtained $\text{Zn}_{1-x}\text{Co}_x\text{O}$ samples corresponds to $x \sim 0.5$. The Raman spectra of such samples correspond to the $\text{Zn}_{1-x}\text{Co}_x\text{O}$ phase at $x \sim 0.5$ [75], as shown in Figure 5 (bottom spectrum).

Surprisingly, the samples that exhibit XRD patterns of the ZnO and Co_3O_4 phases show no known Raman spectra corresponding to the ZnO or Co_3O_4 phases; their spectra are almost identical to the $\text{Zn}_{1-x}\text{Co}_x\text{O}$ samples. This is presumably due to the presence of a thin layer of this phase on the surface of all ZnO or Co_3O_4 nanoparticles. It can be concluded that a layer of h-Zn-Co-O solid solution surrounds these nanoparticles during synthesis and suppresses their further growth, which opens up the possibility of the simple synthesis of nanoparticles with a high yield. The blue laser excitation used in Raman scattering studies has a shallow penetration depth compared to the X-rays used in XRD analysis. With the assumption that the absorption coefficient is not less than $\sim 10^4 \text{ cm}^{-1}$, the estimation of the effective depth of light absorption was 100 nm, while the thickness of ~100 microns of the active layer of the electrode is comparable to the X-ray penetration depth. Therefore, Raman spectra corresponding to ZnO or Co_3O_4 are not observed. Short-term treatment in an alkaline electrolyte modified the spectra (Figure 5, upper spectrum), indicating the instability of the h-Zn-Co-O solid solution in an alkaline environment.

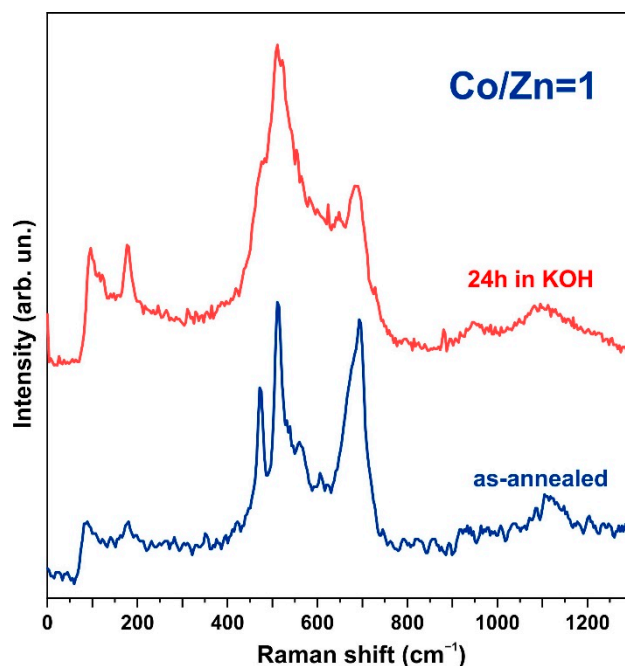


Figure 5. Raman spectra of the h-Zn-Co-O sample after annealing in N₂ (lower spectrum) and after exposure to a 3.5 M KOH solution for 24 h (upper spectrum).

3.3. XPS Spectra

The XPS spectra also indicate degradation of the ZnO phase and the formation of hydroxides. Figures 6–8 show the XPS spectra of the Zn2p, Co2p, and O1s of the h-Zn-Co-O/NF electrode before and after treatment for 10 min in 3.5 M KOH. The intensity of the XPS spectra of Zn2p (Figure 6) decreased significantly after the short-term alkaline treatment, while the change in the intensity of the XPS peaks corresponding to other elements was not significant. Thus, a dramatic decrease in the concentration of zinc atoms in the near-surface region after short-term alkaline etching takes place. Figure 7a demonstrates the Co 2p XPS spectra before and after treatment of the electrode in 3.5 M KOH for 10 min. It is shown that even such short-term alkaline processing causes significant changes to the XPS spectra. Figure 7b shows the decompositions of the Co 2p XPS spectra into three bands, which can be attributed to the Co³⁺ and Co²⁺ charge states and a satellite peak. It can be seen that alkaline treatment causes an increase in the contribution of the Co²⁺ states compared to the Co³⁺ ones, which can be explained by the formation of cobalt hydroxides, where cobalt demonstrates a +2 valency. The XPS spectra of the oxygen (O1s) within the sample, which has been annealed in the air and consists of ZnO and Co₃O₄ phases (Figure 8a), also change significantly after short-term alkaline etching, showing a decrease in the intensity of the line at ~530 eV, which is linked to the presence of lattice oxygen or oxygen in the metal oxide, and an increase in the intensity of the band at ~531.5 eV, which corresponds to the hydroxide (OH)[−] and perhydroxide (OOH)[−] forms of oxygen. This phase change in the structure of the electrode material results in a rapid increase in the electrode's capacitance as discussed in the electrochemical measurements of the electrodes below. The peak at ~533 eV may be due to structural water. Thus, the XPS spectra of O1s indicate that accumulation of hydroxide and perhydroxide forms occur as a result of short-term alkaline etching. The O1s XPS spectra of the sample, which has previously been annealed in hydrogen and consists of the Zn-Co-O solid solution phase (Figure 8b), undergo less pronounced changes after alkaline treatment, since after annealing in hydrogen the 531.5 eV band is already dominant. At the same time, the zinc content in the near-surface areas decreases sharply. This is consistent with the XRD results.

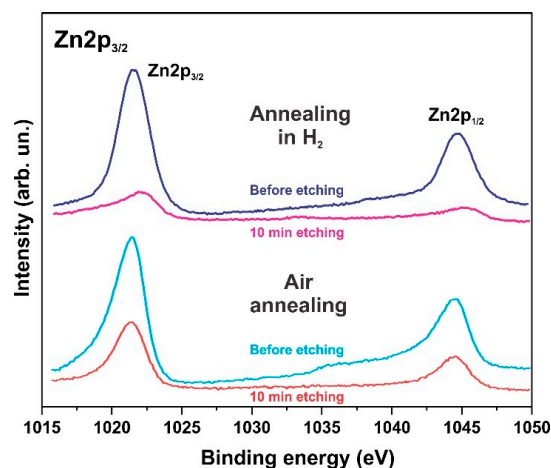


Figure 6. XPS Zn2p spectrum of the h-Zn-Co-O/NF electrodes annealed at 300 °C in either air or H₂ atmosphere followed by treatment for 10 min in 3.5 M KOH.

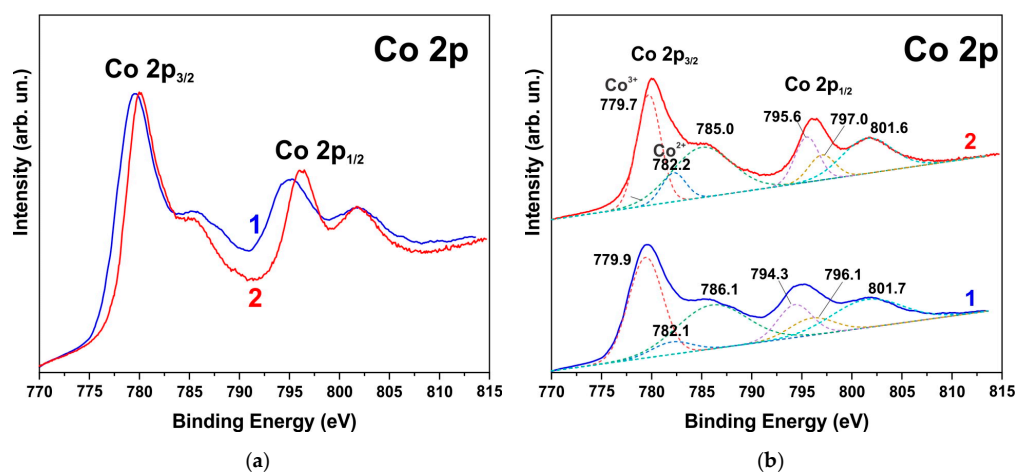


Figure 7. XPS Co2p spectrum of h-Zn-Co-O/NF electrode annealed at 300 °C in air before (1) and after treatment for 10 min in 3.5 M KOH (2) (a) Deconvolution of the same spectra into individual components is shown by dashed lines in red (Co³⁺), blue (Co²⁺), and green (satellite band) colors (b).

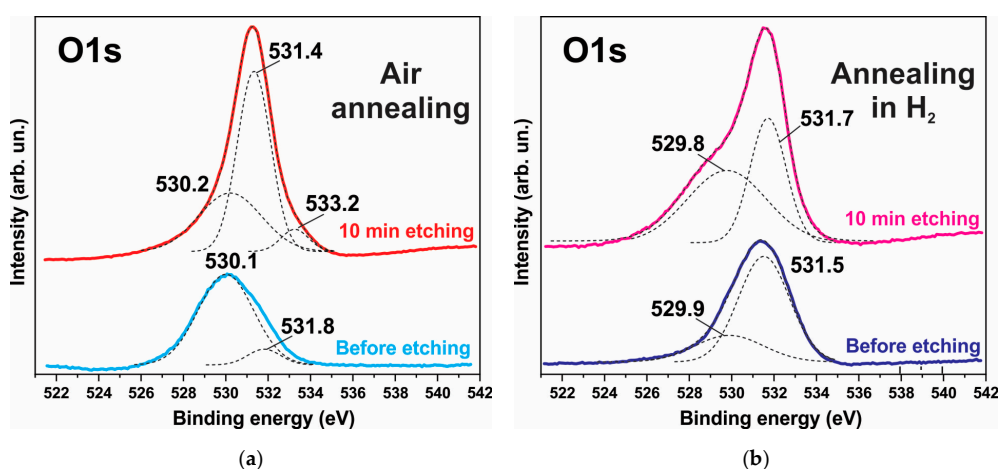


Figure 8. XPS O1s spectrum of the h-Zn-Co-O/NF electrode annealed in either air (a) or H₂ (b) atmosphere before and after treatment for 10 min in 3.5 M KOH. The deconvolution of the spectrum into individual components is shown by the dotted lines.

3.4. Electrochemical Measurements of Electrodes

The electrochemical properties of ZnO-Co₃O₄ and h-Zn-Co-O electrodes are also subject to changes when measurements are carried out on an alkaline electrolyte. The electrochemical characteristics of all of the tested ZnO/Co₃O₄/NF and h-Zn-Co-O/NF electrodes change rapidly during the initial phase of the CV measurement process, as shown in Figures 9a and 10a. Figure 9a shows the CV characteristics of a h-Zn-Co-O electrode prepared by AcCo+NZn synthesis followed by annealing in hydrogen. It can be seen that the electrode's capacitance increases rapidly during the first cycles; the CV characteristics stabilize after approximately 45 cycles or ~18 min of measurements. This increase can be associated with the processes of change in the phase structure of the electrode material, as detected by XRD data after a similar alkaline treatment. That is mainly due to the dissolution of fractions containing Zn, and the formation of cobalt oxide nanoparticles.

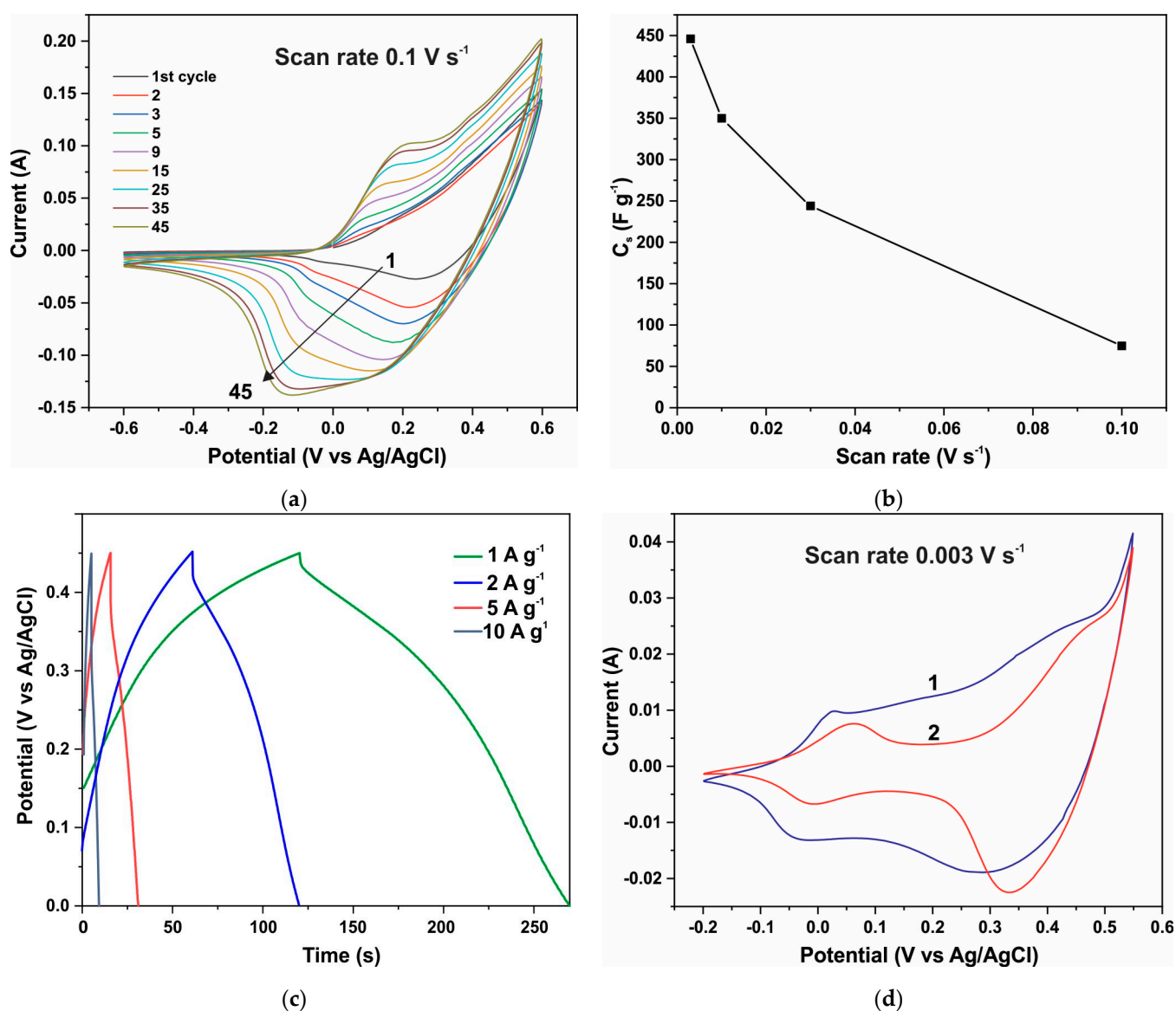


Figure 9. CV curves of the h-Zn-Co-O/NF electrode during the first 45 CV cycles at a speed of 0.1 V s⁻¹ (a); specific capacitance versus scanning speed of CV curves (b); GCD curves after establishing stationary CV curves (c); CV curves after stabilization of characteristics (curve 1) and after a week of aging in air (curve 2) (d).

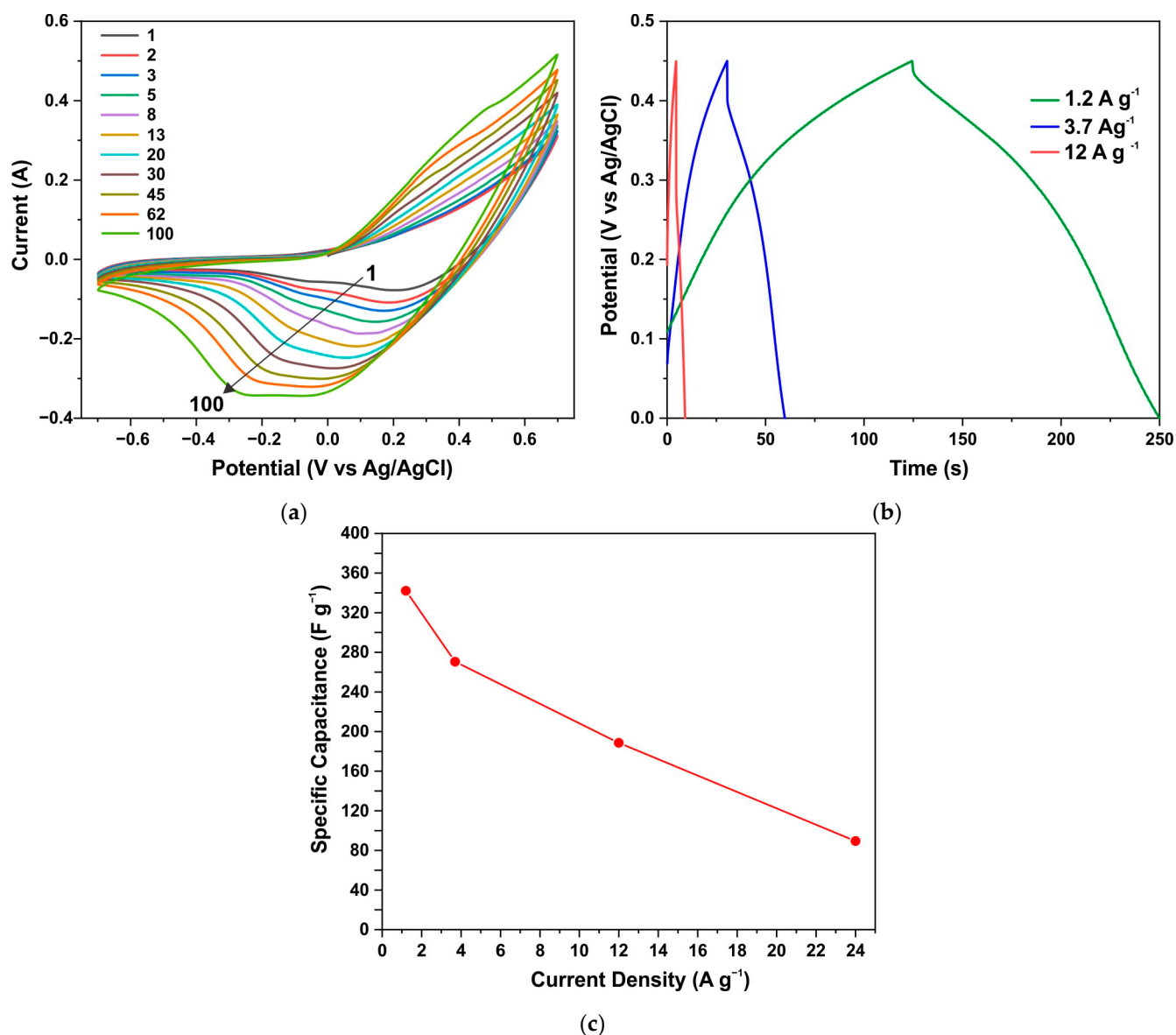


Figure 10. CV curves of the ZnO/Co₃O₄/NF electrode annealed in air during the first 100 cycles at a speed of 0.3 V s⁻¹ (a); GCD curves after establishing stationary CV curves (b); specific capacitance vs. current density (c).

After the stabilization of its characteristics, the capacitance of an electrode with the area of 1 cm² and a mass of 0.0105 g reached a value of 4.689 F after ~18 min cycling at a scanning speed of 0.003 V s⁻¹ (Figure 9b). This translates to a specific capacitance of 446 F g⁻¹ when the capacitance is measured using the CV method. The specific capacitance determined by the GCD method at a current of 1 A g⁻¹ (Figure 9c) was 345 F g⁻¹. Figure 9d shows the CV characteristics of this electrode, with curve 1 corresponding to the measurement after stabilization, where its shape is close to rectangular along with the main contribution of the redox reactions Co³⁺ ↔ Co⁴⁺ at high potentials of ~0.4 V vs. Ag/AgCl, (a potential range between 0.32 to 0.45 V) and a significant current contribution at low potentials of ~-0.75 V vs. Ag/AgCl, (a potential range of ±0.5V) [76,77]. These reactions correspond to Co²⁺ ↔ Co³⁺ reactions involving less oxidized divalent cobalt and hydroxyl groups, the presence of which is already indicated by the XRD and XPS results (Figure 1, Figure 4, and Figure 7). However, after aging in the air for 7 days, repeated CV measurements (curve 2) of this electrode show that the capacitance decreases significantly to 3.038 Farads (~289 F g⁻¹) when it is measured using the CV method. From Figure 9d, it can be seen that the capacity

decreases due to the decrease in the concentration of low-potential redox species. It can be concluded that these divalent cobalt species are unstable in the air.

Similar results are demonstrated by an electrode from a sample obtained through the synthesis of AcCo+NZn followed by annealing in air. Figure 10a shows the CV characteristics for such an electrode measured during the first 100 cycles at a scan rate of 0.3 V s^{-1} . Here the capacitance also increases significantly during CV measurements until stationary CV curves were obtained after ~ 15 min of measurements. Figure 10b,c show the GCD curves and specific capacitance versus current density for the annealed AcCo+NZn electrode, respectively. The specific capacitance measured using the GCD method at a current density of 1.2 A g^{-1} was 341 F g^{-1} and this decreased to 89 F g^{-1} at a current of 12 A g^{-1} .

The increase in capacitance during CV measurements can be due to several reasons. Capacitance can increase due to an enhanced surface area of the electrode being wetted by the electrolyte solution. This is mainly because of the existence of a smaller hydrophilic surface area on the fresh electrode. Capacitance can also increase when the surface is activated during electrochemical redox cycling. It is noteworthy that, when using a Co_3O_4 sample grown under the same conditions but without the addition of zinc precursors, the CV characteristics quickly reached stationary values, and the effect of increasing capacity during cycling was insignificant. The increase in capacitance over ~ 20 min, shown in Figures 9 and 10, can be attributed to the processes of the phase change that occur in the electrode material when it is exposed to the electrolyte. Such changes are confirmed by the XRD data for samples treated in the electrolyte for a similar time.

Thus, the electrode capacity increases due to both surface activation as well as the dissolution of ZnO and $\text{Zn}_{1-x}\text{Co}_x\text{O}$. As a result of alkaline etching and the electrochemical redox action, the ZnO and $\text{Zn}_{1-x}\text{Co}_x\text{O}$ fractions disappear, cobalt hydroxides and oxide are formed, and consequently, the main Co_3O_4 phase remains, as indicated by the XRD results (Figure 4b). In this case, the Co_3O_4 phase consists of nanoparticles, since the active material in the electrode is immobilized by a binder, and at room temperature, large Co_3O_4 crystallites cannot form as a result of the alkaline dissolution of ZnO and $\text{Zn}_{1-x}\text{Co}_x\text{O}$. The h-Zn-Co-O phase shell also prevents the formation of large Co_3O_4 particles. Since the structure of manufactured electrodes changes significantly as a result of their operation in an electrolyte, it is necessary to test the electrode for the stability of its parameters during cycling. This is crucial because cobalt oxide undergoes a very significant volumetric change during electrochemical oxidation–reduction [41–47], which causes the degradation of the properties of electrodes.

3.5. Electrochemical Measurements of a Hybrid Capacitor

The cyclic stability of the resulting electrodes was studied in a typical hybrid capacitor, using a positive h-Zn-Co-O/NF electrode made from the obtained material, and an AC/NF negative electrode. Figures S2–S6 show the electrochemical characteristics of the hybrid capacitor. Cyclic voltammetry curves measured in a three-electrode configuration at a scan rate of 0.01 V s^{-1} for a positive electrode with an active mass of 0.025 g and a negative AC/NF electrode are shown in Figure S2. The CV curves of a h-Zn-Co-O/AC/NF capacitor composed of these electrodes are shown in Figures S3 and S4. The CV curves are measured by varying the scan rate and potential range. GCD curves of the h-Zn-Co-O/AC/NF capacitor at different voltage ranges are shown in Figure S5a. Increasing the potential from 0.8 V to 1.6 V resulted in a linear increase in capacitance (Figure S5b).

The GCD curves (Figure S6a) demonstrate a close-to-linear change in potential over time, characteristic of supercapacitors at a fixed charge/discharge current. The relatively rapid drop in capacitance with the increase in current (Figure S6b) is presumably related to the diffusion nature of the current and the series resistance of the capacitor which was 0.2 Ohm (Figure S7). The Nyquist plot also shows that, at a bias of 1.4 V, the capacitor leakage currents are already significant (Figure S7). So, the operating voltage of the capacitor was between 1.2 and 1.4 V.

The cyclic stability of the h-Zn-Co-O/AC/NF capacitor is shown as a plot of discharge time (dt) versus cycle number (Figure 11a). Figure 11b shows the charge/discharge curves of the 100th, 3300th, and 5000th cycles. It can be seen that the capacitance increases at the initial stage, and ~1000 charge/discharge cycles are required to stabilize. After 10,000 cycles, the h-Zn-Co-O/AC/NF capacitor retains 87% of its maximum capacitance, indicating the high stability of the electrode structure consisting of cobalt oxide nanoparticles formed from the h-Zn-Co-O/NF system as a result of both alkaline etching and the in situ electrochemical redox process.

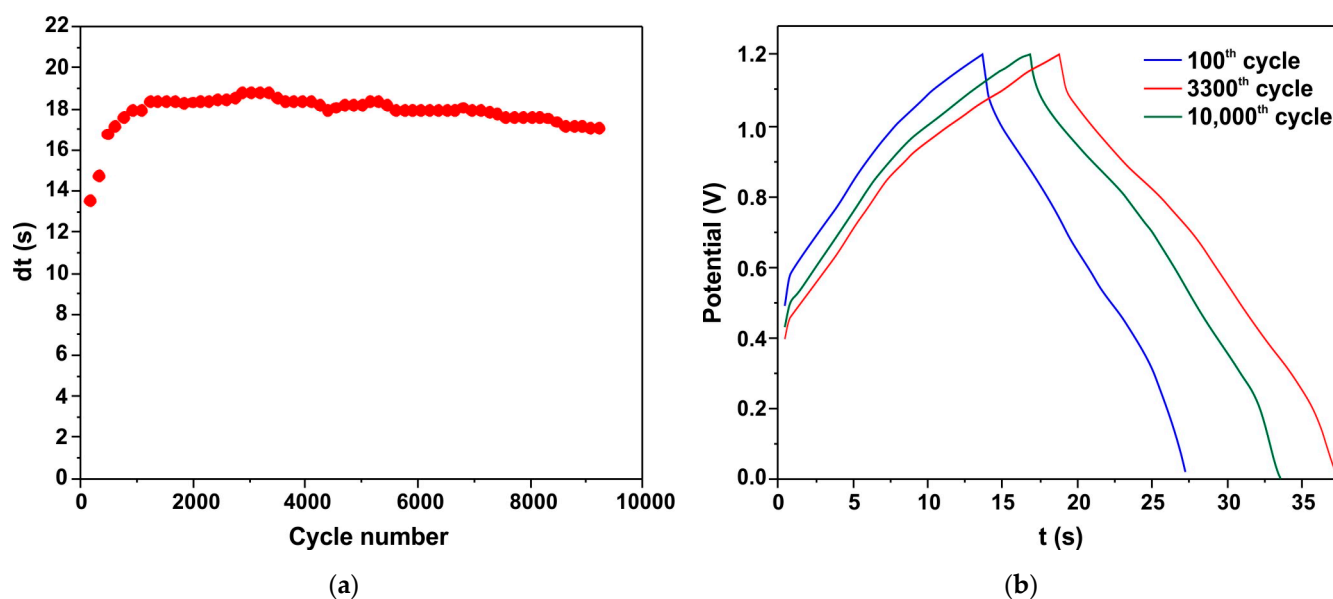


Figure 11. Cyclic stability of the h-Zn-Co-O/AC/NF capacitor as shown by the discharge time (a). The C/D curves of the 100th, 3300th, and 10,000th cycles (b).

4. Conclusions

In this work, changes in the structures and properties changes of the materials and electrodes used in ZnO-based supercapacitors, such as ZnO-Co₃O₄ composites and Zn_{1-x}Co_xO solid solutions with a hexagonal structure, have been studied. It has been shown that, when using an alkaline electrolyte of 3.5 M KOH, the structure of the electrodes rapidly changes; in the initial stage, the ZnO content in the ZnO-Co₃O₄ and h-Zn-Co-O composites decreases, and the Zn_{1-x}Co_xO solid solutions decompose with the appearance of hydroxides Co(OH)₂ and Zn₂Co₃(OH)₁₀·2H₂O, where long-term electrochemical cycling leads to the formation of the Co₃O₄ main phase. These results must be taken into account when manufacturing supercapacitors using ZnO composite electrodes since, even with a limited volume of alkaline electrolyte, the surface and near-surface layers of the electrode, which determine the capacitive properties of the supercapacitor, will be subject to chemical and electrochemical corrosion. Because the active material in the electrodes is immobilized on the substrate, as a result of in situ electrochemical action on the ZnO-Co₃O₄ and h-Zn-Co-O systems, Co₃O₄ nanoparticles are formed with a high specific surface area, which is activated by the in situ formation process. This ensures a high specific capacitance of the electrodes, high charge/discharge currents, and long-term stability during cyclic operation. Therefore, the formation of supercapacitor electrodes from ZnO-Co₃O₄ composites and Zn_{1-x}Co_xO solid solutions with subsequent removal of the zinc-containing fraction during in situ electrochemical processing is a simple method for the formation of an electrode using nanostructured cobalt oxide. This method does not require special measures for the formation of nanosized cobalt oxide particles, since, during synthesis, the Zn_{1-x}Co_xO layers envelop the cobalt oxide particles and prevent their growth. The method does not require high-temperature treatments. It may also be promising to use the resulting material

immediately after synthesis when cobalt oxide nanoparticles can be obtained by in situ processing. However, the development of a suitable high-conductivity matrix to achieve a low series resistance is crucial in the future.

Supplementary Materials: The following supporting information can be downloaded at: <https://www.mdpi.com/article/10.3390/en17081888/s1>, Figure S1: XRD data of the ZnO+Co₃O₄ sample after AcZn+AcCo synthesis and annealing at 450 °C in air (1); the same sample after subsequent etching in 3.5 M KOH for 40 min (2); Figure S2: CV curves of h-Zn-Co-O/NF sample with an active mass of 0.025 g as the positive electrode and an AC/NF sample as negative electrode. CV curves were recorded in a three-electrode system at a scan rate of 0.01 V s⁻¹; Figure S3: CV curves of h-Zn-Co-O/AC/NF capacitor at different scan rates of 0.01–0.3 V s⁻¹; Figure S4: CV curves of the h-Zn-Co-O/AC/NF capacitor at different voltage windows, and at 0.1 V s⁻¹ scan rate; Figure S5: GCD curves of the h-Zn-Co-O/AC/NF capacitor at different operating potential windows, and at current of 32 mA (a); Plot of the capacity obtained from the GCD curves versus the operating potential window (b); Figure S6: GCD curves of the h-Zn-Co-O/AC/NF capacitor at different current (a); Capacitance vs. current (b); Figure S7: Nyquist plots of the h-Zn-Co-O/AC/NF capacitor in the frequency range of 0.003–5 × 10³ Hz at various capacitor voltages; the inset indicates the Nyquist plots in the high-frequency region.

Author Contributions: Conceptualization, K.A., Z.K. and M.M.; methodology, K.A., Z.K. and M.M.; validation, K.A., Z.K. and M.M.; investigation, K.A., Z.K., V.K., K.Y. and D.B.; writing—original draft preparation, K.A., Z.K. and M.M.; writing—review and editing, K.A., Z.K. and M.M.; supervision, K.A. and M.G.; project administration, K.A. and M.G.; funding acquisition, A.S. All authors have read and agreed to the published version of the manuscript.

Funding: This research was funded by the Ministry of Science and Higher Education of the Republic of Kazakhstan, grant number BR18574141.

Data Availability Statement: The original contributions presented in the study are included in the article/supplementary material, further inquiries can be directed to the corresponding authors.

Conflicts of Interest: The authors declare no conflicts of interest. The funders had no role in the design of the study; in the collection, analyses, or interpretation of data; in the writing of the manuscript; or in the decision to publish the results.

References

1. Wisz, G.; Virt, I.; Sagan, P.; Potera, P.; Yavorskyi, R. Structural, Optical and Electrical Properties of Zinc Oxide Layers Produced by Pulsed Laser Deposition Method. *Nanoscale Res. Lett.* **2017**, *12*, 253. [[CrossRef](#)] [[PubMed](#)]
2. Vyas, S. A Short Review on Properties and Applications of Zinc Oxide Based Thin Films and Devices. *Johns. Matthey Technol. Rev.* **2020**, *64*, 202–218. [[CrossRef](#)]
3. Vayssieres, L.; Keis, K.; Hagfeldt, A.; Lindquist, S.-E. Three-Dimensional Array of Highly Oriented Crystalline ZnO Microtubes. *Chem. Mater.* **2001**, *13*, 4395–4398. [[CrossRef](#)]
4. Zhao, Y.; Tong, F.; Wang, M.H. Effect of cobalt doping on microstructures and dielectric properties of ZnO. *Can. J. Chem.* **2019**, *97*, 227–232. [[CrossRef](#)]
5. Arshad, M.; Ansari, M.M.; Ahmed, A.S.; Tripathi, P.; Ashraf, S.; Naqvi, A.; Azam, A. Band gap engineering and enhanced photoluminescence of Mg doped ZnO nanoparticles synthesized by wet chemical route. *J. Lumin.* **2015**, *161*, 275–280. [[CrossRef](#)]
6. Hassan, M.M.; Khan, W.; Azam, A.; Naqvi, A. Influence of Cr incorporation on structural, dielectric and optical properties of ZnO nanoparticles. *J. Ind. Eng. Chem.* **2015**, *21*, 283–291. [[CrossRef](#)]
7. Gürbüz, O.; Okutan, M. Structural, electrical, and dielectric properties of Cr doped ZnO thin films: Role of Cr concentration. *Appl. Surf. Sci.* **2016**, *387*, 1211–1218. [[CrossRef](#)]
8. Tabib, A.; Sdiri, N.; Elhouichet, H.; Férid, M. Investigations on electrical conductivity and dielectric properties of Na doped ZnO synthesized from sol gel method. *J. Alloy. Compd.* **2015**, *622*, 687–694. [[CrossRef](#)]
9. Vladut, C.M.; Mihaiu, S.; Mocioiu, O.C.; Atkinson, I.; Pandelescu, J.; Anghel, E.M.; Calderon-Moreno, J.M.; Zaharescu, M. Thermal studies of Mn²⁺-doped ZnO powders formation by sol-gel method. *J. Therm. Anal. Calorim.* **2019**, *135*, 2943–2951. [[CrossRef](#)]
10. Han, C.; Duan, L.; Zhao, X.; Hu, Z.; Niu, Y.; Geng, W. Effect of Fe doping on structural and optical properties of ZnO films and nanorods. *J. Alloy. Compd.* **2019**, *770*, 854–863. [[CrossRef](#)]
11. Raha, S. Ahmaruzzaman ZnO nanostructured materials and their potential applications: Progress, challenges and perspectives. *Nanoscale Adv.* **2022**, *4*, 1868–1925. [[CrossRef](#)]

12. Clarke, B.; Ghandi, K. The Interplay of Growth Mechanism and Properties of ZnO Nanostructures for Different Applications. *Small* **2023**, *19*, e2302864. [[CrossRef](#)]
13. Wang, J.; Chen, R.; Xiang, L.; Komarneni, S. Synthesis, properties and applications of ZnO nanomaterials with oxygen vacancies: A review. *Ceram. Int.* **2018**, *44*, 7357–7377. [[CrossRef](#)]
14. Theerthagiri, J.; Salla, S.; Senthil, R.A.; Nithyadharseni, P.; Madankumar, A.; Arunachalam, P.; Maiyalagan, T.; Kim, H.-S. A review on ZnO nanostructured materials: Energy, environmental and biological applications. *Nanotechnology* **2019**, *30*, 392001. [[CrossRef](#)] [[PubMed](#)]
15. Yin, X.; Hua, Y.; Gao, Z. Two-Dimensional Materials for High-Performance Oxygen Evolution Reaction: Fundamentals, Recent Progress, and Improving Strategies. *Renewables* **2023**, *1*, 190–226. [[CrossRef](#)]
16. Goktas, S.; Goktas, A. A comparative study on recent progress in efficient ZnO based nanocomposite and heterojunction photocatalysts: A review. *J. Alloy. Compd.* **2021**, *863*, 158734. [[CrossRef](#)]
17. Mehr, M.E.; Maleki-Ghaleh, H.; Yarahmadi, M.; Kavanlouei, M.; Siadati, M.H. Synthesis and characterization of photocatalytic zinc oxide/titanium oxide (core/shell) nanocomposites. *J. Alloy. Compd.* **2021**, *882*, 160777. [[CrossRef](#)]
18. Bakranova, D.; Seitov, B.; Bakranov, N. Preparation and Photocatalytic/Photoelectrochemical Investigation of 2D ZnO/CdS Nanocomposites. *Chemengineering* **2022**, *6*, 87. [[CrossRef](#)]
19. Seitov, B.; Kurbanbekov, S.; Bakranova, D.; Abdylidayeva, N.; Bakranov, N. Study of the Photoelectrochemical Properties of 1D ZnO Based Nanocomposites. *Catalysts* **2021**, *11*, 1235. [[CrossRef](#)]
20. Franco, M.A.; Conti, P.P.; Andre, R.S.; Correa, D.S. A review on chemiresistive ZnO gas sensors. *Sensors Actuators Rep.* **2022**, *4*, 100100. [[CrossRef](#)]
21. Kang, Y.; Yu, F.; Zhang, L.; Wang, W.; Chen, L.; Li, Y. Review of ZnO-based nanomaterials in gas sensors. *Solid State Ionics* **2021**, *360*, 115544. [[CrossRef](#)]
22. Krishna, K.G.; Umadevi, G.; Parne, S.; Pothukanuri, N. Zinc oxide based gas sensors and their derivatives: A critical review. *J. Mater. Chem. C* **2023**, *11*, 3906–3925. [[CrossRef](#)]
23. Ivanishcheva, A.P.; Sysoev, V.V.; Abdullin, K.A.; Nesterenko, A.V.; Khubezhov, S.A.; Petrov, V.V. The Application of Combined Visible and Ultraviolet Irradiation to Improve the Functional Characteristics of Gas Sensors Based on ZnO/SnO₂ and ZnO/Au Nanorods. *Chemosensors* **2023**, *11*, 200. [[CrossRef](#)]
24. Shanmugam, N.R.; Muthukumar, S.; Prasad, S. A review on ZnO-based electrical biosensors for cardiac biomarker detection. *Futur. Sci. OA* **2017**, *3*, FSO196. [[CrossRef](#)] [[PubMed](#)]
25. Napi, M.L.M.; Sultan, S.M.; Ismail, R.; How, K.W.; Ahmad, M.K. Electrochemical-Based Biosensors on Different Zinc Oxide Nanostructures: A Review. *Materials* **2019**, *12*, 2985. [[CrossRef](#)]
26. Napi, M.L.M.; Noorden, A.F.A.; Tan, M.L.P.; Jamaluddin, H.; Hamid, F.A.; Hashim, U.; Ahmad, M.R.; Sultan, S.M. Review—Three Dimensional Zinc Oxide Nanostructures as an Active Site Platform for Biosensor: Recent Trend in Healthcare Diagnosis. *J. Electrochem. Soc.* **2020**, *167*, 137501. [[CrossRef](#)]
27. Krishna, M.S.; Singh, S.; Batool, M.; Fahmy, H.M.; Seku, K.; Shalan, A.E.; Lanceros-Mendez, S.; Zafar, M.N. A review on 2D-ZnO nanostructure based biosensors: From materials to devices. *Mater. Adv.* **2023**, *4*, 320–354. [[CrossRef](#)]
28. Rodrigues, J.; Pereira, S.O.; Zaroni, J.; Rodrigues, C.; Brás, M.; Costa, F.M.; Monteiro, T. ZnO Transducers for Photoluminescence-Based Biosensors: A Review. *Chemosensors* **2022**, *10*, 39. [[CrossRef](#)]
29. Tripathy, N.; Kim, D.-H. Metal oxide modified ZnO nanomaterials for biosensor applications. *Nano Converg.* **2018**, *5*, 27. [[CrossRef](#)]
30. Paltusheva, Z.U.; Ashikbayeva, Z.; Tosi, D.; Gritsenko, L.V. Highly Sensitive Zinc Oxide Fiber-Optic Biosensor for the Detection of CD44 Protein. *Biosensors* **2022**, *12*, 1015. [[CrossRef](#)]
31. Bakranova, D.; Seitov, B.; Bakranov, N. Photocatalytic and Glucose Sensing Properties of ZnO-Based Nanocoating. *Chemengineering* **2023**, *7*, 22. [[CrossRef](#)]
32. Rekha, S.M.; Neelamana, H.V.; Bhat, S.V. Recent Advances in Solution-Processed Zinc Oxide Thin Films for Ultraviolet Photodetectors. *ACS Appl. Electron. Mater.* **2023**, *5*, 4051–4066. [[CrossRef](#)]
33. Boruah, B.D. Zinc oxide ultraviolet photodetectors: Rapid progress from conventional to self-powered photodetectors. *Nanoscale Adv.* **2019**, *1*, 2059–2085. [[CrossRef](#)] [[PubMed](#)]
34. Liu, K.; Sakurai, M.; Aono, M. ZnO-Based Ultraviolet Photodetectors. *Sensors* **2010**, *10*, 8604–8634. [[CrossRef](#)] [[PubMed](#)]
35. Nandi, S.; Kumar, S.; Misra, A. Zinc oxide heterostructures: Advances in devices from self-powered photodetectors to self-charging supercapacitors. *Mater. Adv.* **2021**, *2*, 6768–6799. [[CrossRef](#)]
36. Shang, S.; Dong, Y.; Zhang, W.; Ren, W. Fabrication and Performance of UV Photodetector of ZnO Nanorods Decorated with Al Nanoparticles. *Nanomaterials* **2022**, *12*, 3768. [[CrossRef](#)] [[PubMed](#)]
37. Young, S.-J.; Liu, Y.-H.; Shiblee, M.D.N.I.; Ahmed, K.; Lai, L.-T.; Nagahara, L.; Thundat, T.; Yoshida, T.; Arya, S.; Furukawa, H.; et al. Flexible Ultraviolet Photodetectors Based on One-Dimensional Gallium-Doped Zinc Oxide Nanostructures. *ACS Appl. Electron. Mater.* **2020**, *2*, 3522–3529. [[CrossRef](#)]
38. Wibowo, A.; Marsudi, M.A.; Amal, M.I.; Ananda, M.B.; Stephanie, R.; Ardy, H.; Diguna, L.J. ZnO nanostructured materials for emerging solar cell applications. *RSC Adv.* **2020**, *10*, 42838–42859. [[CrossRef](#)] [[PubMed](#)]
39. Consonni, V.; Briscoe, J.; Kärber, E.; Li, X.; Cossuet, T. ZnO nanowires for solar cells: A comprehensive review. *Nanotechnology* **2019**, *30*, 362001. [[CrossRef](#)]

40. Peksu, E.; Coskun, A.; Karaagac, H. Recent progress in solar cells based on one dimensional ZnO nanostructures. *Nanotechnology* **2023**, *34*, 352003. [[CrossRef](#)]
41. Wang, L.-H.; Ren, L.-L.; Qin, Y.-F. The Review of Hybridization of Transition Metal-Based Chalcogenides for Lithium-Ion Battery Anodes. *Materials* **2023**, *16*, 4448. [[CrossRef](#)] [[PubMed](#)]
42. Gonçalves, J.M.; da Silva, M.I.; Silva, M.N.T.; Martins, P.R.; Nossol, E.; Toma, H.E.; Angnes, L. Recent progress in ZnCo₂O₄ and its composites for energy storage and conversion: A review. *Energy Adv.* **2022**, *1*, 793–841. [[CrossRef](#)]
43. Najib, S.; Erdem, E. Current progress achieved in novel materials for supercapacitor electrodes: Mini review. *Nanoscale Adv.* **2019**, *1*, 2817–2827. [[CrossRef](#)] [[PubMed](#)]
44. Forouzandeh, P.; Kumaravel, V.; Pillai, S.C. Electrode Materials for Supercapacitors: A Review of Recent Advances. *Catalysts* **2020**, *10*, 969. [[CrossRef](#)]
45. Nandi, D.; Mohan, V.B.; Bhowmick, A.K.; Bhattacharyya, D. Metal/metal oxide decorated graphene synthesis and application as supercapacitor: A review. *J. Mater. Sci.* **2020**, *55*, 6375–6400. [[CrossRef](#)]
46. Yan, Z.; Sun, Z.; Yue, K.; Li, A.; Qian, L. CoO/ZnO nanoclusters immobilized on N-doped 3 D reduced graphene oxide for enhancing lithium storage capacity. *J. Alloy. Compd.* **2020**, *836*, 155443. [[CrossRef](#)]
47. Abebe, E.M.; Ujihara, M. Influence of Temperature on ZnO/Co₃O₄ Nanocomposites for High Energy Storage Supercapacitors. *ACS Omega* **2021**, *6*, 23750–23763. [[CrossRef](#)] [[PubMed](#)]
48. Angelin, M.D.; Rajkumar, S.; Ravichandran, A.; Merlin, J.P. Systematic investigation on the electrochemical performance of Cd-doped ZnO as electrode material for energy storage devices. *J. Phys. Chem. Solids* **2021**, *161*, 110486. [[CrossRef](#)]
49. Zhou, H.; Fu, W.; Muhammad, M.; Xie, M.; Xie, E.; Han, W.-H. Self-assembled microspheres composed of porous ZnO/CoO nanosheets for aqueous hybrid supercapacitors. *J. Phys. D Appl. Phys.* **2019**, *52*, 505501. [[CrossRef](#)]
50. Alver, U.; Tanrıverdi, A. Boron doped ZnO embedded into reduced graphene oxide for electrochemical supercapacitors. *Appl. Surf. Sci.* **2016**, *378*, 368–374. [[CrossRef](#)]
51. Shaheen, I.; Ahmad, K.S.; Zequine, C.; Gupta, R.K.; Thomas, A.G.; Malik, M.A. Sustainable synthesis of organic framework-derived ZnO nanoparticles for fabrication of supercapacitor electrode. *Environ. Technol.* **2022**, *43*, 605–616. [[CrossRef](#)]
52. Najib, S.; Bakan, F.; Abdullayeva, N.; Bahariqushchi, R.; Kasap, S.; Franzò, G.; Sankir, M.; Sankir, N.D.; Mirabella, S.; Erdem, E. Tailoring morphology to control defect structures in ZnO electrodes for high-performance supercapacitor devices. *Nanoscale* **2020**, *12*, 16162–16172. [[CrossRef](#)]
53. Pradeeswari, K.; Venkatesan, A.; Pandi, P.; Karthik, K.; Krishna, K.V.H.; Kumar, R.M. Study on the electrochemical performance of ZnO nanoparticles synthesized via non-aqueous sol-gel route for supercapacitor applications. *Mater. Res. Express* **2019**, *6*, 105525. [[CrossRef](#)]
54. Reddy, I.N.; Reddy, C.V.; Sreedhar, A.; Shim, J.; Cho, M.; Yoo, K.; Kim, D. Structural, optical, and bifunctional applications: Supercapacitor and photoelectrochemical water splitting of Ni-doped ZnO nanostructures. *J. Electroanal. Chem.* **2018**, *828*, 124–136. [[CrossRef](#)]
55. Erdemir, F.; Tuzcu, E.; Bilgin, S.; Alver, Ü.; Çanakçı, A. Influence of fluorine doping of zinc oxide on its electrochemical performance in supercapacitors. *Mater. Chem. Phys.* **2021**, *259*, 124033. [[CrossRef](#)]
56. Ali, A.; Ammar, M.; Ali, M.; Yahya, Z.; Javaid, M.Y.; Hassan, S.U.; Ahmed, T. Mo-doped ZnO nanoflakes on Ni-foam for asymmetric supercapacitor applications. *RSC Adv.* **2019**, *9*, 27432–27438. [[CrossRef](#)]
57. Pallavolu, M.R.; Nallapureddy, J.; Nallapureddy, R.R.; Neelima, G.; Yedluri, A.K.; Mandal, T.K.; Pejjai, B.; Joo, S.W. Self-assembled and highly faceted growth of Mo and V doped ZnO nanoflowers for high-performance supercapacitors. *J. Alloy. Compd.* **2021**, *886*, 161234. [[CrossRef](#)]
58. Huang, Y.-Y.; Lin, L.-Y.; Li, X. Efficient battery supercapacitor hybrid devices with quaternary metal oxide electrodes based on nickel and cobalt. *J. Energy Storage* **2019**, *25*, 100826. [[CrossRef](#)]
59. Radhamani, A.V.; Shareef, K.M.; Rao, M.S.R. ZnO@MnO₂ Core-Shell Nanofiber Cathodes for High Performance Asymmetric Supercapacitors. *ACS Appl. Mater. Interfaces* **2016**, *8*, 30531–30542. [[CrossRef](#)]
60. Huang, M.; Li, F.; Zhao, X.L.; Luo, D.; You, X.Q.; Zhang, Y.X.; Li, G. Hierarchical ZnO@MnO₂ Core-Shell Pillar Arrays on Ni Foam for Binder-Free Supercapacitor Electrodes. *Electrochimica Acta* **2015**, *152*, 172–177. [[CrossRef](#)]
61. Tajik, S.; Dubal, D.P.; Gomez-Romero, P.; Yadegari, A.; Rashidi, A.; Nasernejad, B.; Inamuddin; Asiri, A.M. Nanostructured mixed transition metal oxides for high performance asymmetric supercapacitors: Facile synthetic strategy. *Int. J. Hydrogen Energy* **2017**, *42*, 12384–12395. [[CrossRef](#)]
62. Dutta, A.; Chatterjee, K.; Mishra, S.; Saha, S.K.; Akhtar, A.J. An insight into the electrochemical performance of cobalt-doped ZnO quantum dot for supercapacitor applications. *J. Mater. Res.* **2022**, *37*, 3955–3964. [[CrossRef](#)]
63. He, Y.; Xie, L.; Ding, S.; Long, Y.; Zhou, X.; Hu, Q.; Lin, D. Core-shell nanostructured Zn-Co-O@CoS arrays for high-performance hybrid supercapacitors. *Dalton Trans.* **2021**, *50*, 4923–4931. [[CrossRef](#)]
64. He, Y.; Zhou, X.; Ding, S.; Hu, Q.; Lin, D.; Wei, X. ZnO/CoO@NiCoS nanohybrids with double heterogeneous interface for high-performance hybrid supercapacitors. *J. Alloy. Compd.* **2021**, *875*, 160046. [[CrossRef](#)]
65. Kumar, S.; Ahmed, F.; Shaalan, N.M.; Arshi, N.; Dalela, S.; Chae, K.H. Influence of Fe Doping on the Electrochemical Performance of a ZnO-Nanostructure-Based Electrode for Supercapacitors. *Nanomaterials* **2023**, *13*, 2222. [[CrossRef](#)] [[PubMed](#)]

66. Zenasni, M.; Belhadj, H.; Kiari, M.; Alelyani, M.; Alhailiy, A.B.; Benyoucef, A.; Bakkour, Y. Synthesis, characterization, and enhanced electrochemical behavior of polypyrrole doped ZrO_2 -ZnO electrode materials for supercapacitor applications. *Front. Energy Res.* **2023**, *11*, 1244699. [CrossRef]
67. Ammar, A.U.; Bakan-Misirlioglu, F.; Aleinawi, M.H.; Franzo, G.; Condorelli, G.G.; Yesilbag, F.N.T.; Yesilbag, Y.O.; Mirabella, S.; Erdem, E. All-in-one supercapacitors with high performance enabled by Mn/Cu doped ZnO and MXene. *Mater. Res. Bull.* **2023**, *165*, 112334. [CrossRef]
68. Altaf, C.T.; Colak, T.O.; Rostas, A.M.; Mihet, M.; Lazar, M.D.; Iatsunskyi, I.; Coy, E.; Yildirim, I.D.; Misirlioglu, F.B.; Erdem, E.; et al. GO/ZnO-based all-solid-state photo-supercapacitors: Effect of GO:ZnO ratio on composite properties and device performance. *J. Energy Storage* **2023**, *68*, 107694. [CrossRef]
69. Chauhan, P.S.; Kumar, S.; Mondal, A.; Sharma, P.; Parekh, M.N.; Panwar, V.; Rao, A.M.; Misra, A. Stacked vanadium pentoxide-zinc oxide interface for optically-chargeable supercapacitors. *J. Mater. Chem. A* **2023**, *11*, 95–107. [CrossRef]
70. Mubeen, K.; Shah, M.Z.U.; Sajjad, M.; Irshad, A.; Ali, Z.; Zafar, Z.; Shah, A. Boosting the electrochemical performance of ZnO nanomaterials through a conductive CuS matrix for aqueous supercapacitors. *New J. Chem.* **2023**, *47*, 7819–7829. [CrossRef]
71. Shaheen, I.; Hussain, I.; Zahra, T.; Memon, R.; Alothman, A.A.; Ouladsmane, M.; Qureshi, A.; Niazi, J.H. Electrophoretic Fabrication of ZnO/CuO and ZnO/CuO/rGO Heterostructures-based Thin Films as Environmental Benign Flexible Electrode for Supercapacitor. *Chemosphere* **2023**, *322*, 138149. [CrossRef] [PubMed]
72. Ali, A.; Hameed, I.; Hussain, I.; Mujahid, R.; Ahmad, R.T.M.; Yahya, Z.; Waqas, M.; Ammar, M. High performance asymmetric supercapacitor based on hydrothermally synthesized ZnO nanosheets embedded on Ni foam. *J. Mater. Sci. Mater. Electron.* **2023**, *34*, 744. [CrossRef]
73. Pern, F.J.; To, B.; Glick, S.H.; Sundaramoorthy, R.; DeHart, C.; Glynn, S.; Perkins, C.; Mansfield, L.; Gessert, T. Variations in damp heat-induced degradation behavior of sputtered ZnO window layer for CIGS solar cells. In Proceedings of the Reliability of Photovoltaic Cells, Modules, Components, and Systems III, San Diego, CA, USA, 1–5 August 2010. Available online: <https://www.spiedigitallibrary.org/conference-proceedings-of-spie/7773/1/Variations-in-damp-heat-induced-degradation-behavior-of-sputtered-ZnO/10.1117/12.863078.short> (accessed on 15 November 2023).
74. Chen, A.-L.; Xu, D.; Chen, X.-Y.; Zhang, W.-Y.; Liu, X.-H. Measurements of zinc oxide solubility in sodium hydroxide solution from 25 to 100 °C. *Trans. Nonferrous Met. Soc. China* **2012**, *22*, 1513–1516. [CrossRef]
75. Wang, X.; Xu, J.; Yu, X.; Xue, K.; Yu, J.; Zhao, X. Structural evidence of secondary phase segregation from the Raman vibrational modes in $Zn_{1-x}Co_xO$ ($0 < x < 0.6$). *Appl. Phys. Lett.* **2007**, *91*, 031908. [CrossRef]
76. Pourbaix, M. *Atlas of Electrochemical Equilibria in Aqueous Solutions*, 2nd ed.; NACE International: Brussels, Belgium, 1974.
77. Peek, E.; Åkre, T.; Asselin, E. Technical and business considerations of cobalt hydrometallurgy. *JOM* **2009**, *61*, 43–53. [CrossRef]

Disclaimer/Publisher's Note: The statements, opinions and data contained in all publications are solely those of the individual author(s) and contributor(s) and not of MDPI and/or the editor(s). MDPI and/or the editor(s) disclaim responsibility for any injury to people or property resulting from any ideas, methods, instructions or products referred to in the content.